Lattice Disorder Effect on Magnetic Ordering of Iron Arsenides

A. S. Sefat, X. P. Wang, Y. Liu, D.S. Parker, Q. Zou, M. M. Fu, Z. Gai, G. Kalaiselvan, Y. Vohra, L. Li

¹ Materials Science & Technology Division, Oak Ridge National Laboratory, Oak Ridge, TN 37831
 ² Neutron Scattering Division, Oak Ridge National Laboratory, Oak Ridge, TN 37831
 ³ Center for Nanophase Materials Sciences, Oak Ridge National Laboratory, Oak Ridge, TN 37831, USA
 ⁴ Department of Physics, University of Alabama at Birmingham, Birmingham, AL 35294

This study demonstrates the tuning of Néel temperature via nano- and mesoscale structural features in an iron arsenide. Although magnetic ground states in quantum materials can be theoretically predicted from known crystal structures and chemical compositions, the ordering temperature is harder to pinpoint due to such local lattice variations. In this work we find that a chemically stoichiometric material can order at significantly different Néel antiferromagnetic transition temperatures $(T_{\rm N})$ depending on lattice disorder effects. Here, europium iron-arsenide EuFe₂As₂ crystal, which is a '122' parent of iron arsenide superconductors, is controlled through synthesis to have ordering below $T_N = 195$ K or $T_N = 175$ K due to Fe ordering. In the higher T_N crystals, there are shorter planar Fe-Fe bonds [2.7692(2) Å vs. 2.7745(3) Å], a randomized inplane defect structure, and diffuse scattering along the [00L] crystallographic direction that manifests as a rather broad specific heat peak. For the lower T_N crystals, the a-lattice parameter is larger and the in-plane microscopic structure shows defect ordering along the antiphase boundaries, giving a sharper T_N and a higher superconducting temperature (T_c) upon the application of pressure. First-principles calculations find a strong interaction between c-axis strain and interlayer magnetic coupling, but little impact of planar strain on the magnetic order. Neutron single-crystal diffraction shows that the low-temperature magnetic phase transition due to localized Eu moments is not lattice sensitive, unlike the higher-temperature Fe sublattice ordering. This study demonstrates tunable interactions between lattice disorder and the Néel temperature in a layered quantum material.

A bulk macroscopic magnetic transition in a quantum material is thermally-driven by spin interactions dictated by the nano- and mesoscale structures (e.g., lattice composition, crystal structure, disorder and defects, lattice strain, chemical impurities and dopants). The parents of iron-based superconductors with AFe_2As_2 (A = Ba, Sr, Ca, Eu) formula, known as '122', are semi-metallic with all five Fe 3*d*-bands crossing the Fermi level [1]. The 122s have tetragonal structure at room temperature ($a=b\neq c$), and at a Néel antiferromagnetic transition temperature (T_N) there is a small tetragonal-to-orthorhombic structural distortion (T_s) where the unit cell rotates by ~ 45° within the *ab*-plane, instigating the possibility for twinned domains [2,3]. Below T_N there is a sinusoidal modulation of Fe moments in the form of spin-density wave (SDW) [3] described by a wave vector $q=(\frac{1}{2}\frac{1}{2}1)$ in the tetragonal structure, matching the nesting vector between the electron and hole pockets at Fermi surface [4], and the Fe spin lattice arrangement is a 'stripe' (spins are antiparallel along *a*- and *c*-axes, and parallel along *b*-axis) [5-8].

It is evident that strain can induce a nematic phase transition in 122s [9] that is seen as an electronic in-plane anisotropy [10], driven by orbital (unequal occupation of d_{xz} and d_{yz}) or spin directional order (not long range) that cause breaking of the in-plane C4 rotational symmetry that can split T_N and T_s transitions. Moreover, higher T_N in BaFe₂As₂ is linked to a more homogenous electronic structure [11-14], and there are local structure variations [3]. For SrFe₂As₂, in addition to a large variability of T_N values (195 to 220 K) [13,15,16], superconductivity ($T_c = 21$ K) can be found in strained crystals [17]. Furthermore, CaFe₂As₂ can be synthesized as a non-magnet or an antiferromagnet with a large T_N , achieved by staggered alleviation of Fe–As bonds with thermal annealing [13,18,19]. For this study, we hypothesize that the local lattice details of EuFe₂As₂ affect its T_N value. EuFe₂As₂ is special among the 122s for having SDW order of Fe, in addition to Eu local moments below 20 K with q=(0 0 L) in the orthorhombic structure [20-23]. The Eu local moments are weakly coupled to the Fe sublattice and are strong enough for a large and indirect spin-lattice coupling that can lead to a structural detwinning by a small magnetic field [24], and they cause re-entrant superconductivity [25, 26].

We have produced two stoichiometric EuFe₂As₂ crystals with onset of Fe ordering at $T_N = 195$ K or $T_N = 175$ K, and use X-ray and neutron diffraction, microscopy and spectroscopy techniques to understand chemical and electronic structure features that give these ordering temperatures. Surprisingly, the higher T_N crystal has a broader (usually associated with strain and disorder) specific heat peak, while the lower T_N crystal has a sharp peak. How does T_N relate to lattice and topological features, and does T_N value correlate with averaged lattice parameters? Would higher T_N mean more homogeneous electronic structure? Does the peak shape of specific heat matter? What are the pressure results for diminishing antiferromagnetism and potentially deriving superconductivity in each of these crystals? Our results show that although $T_{N(Fe)}$ and T_c values are greatly sensitive to the planar lattice details and local arrangements of defect structures, Eu ordering is untouched at $T_{N(Eu)} \approx 21$ K. This study documents the variety of ordering temperatures that may be possible in a stoichiometric quantum material due to lattice disorder.

The single crystals of EuFe₂As₂ were grown out of a mixture of Eu and FeAs excess used as liquid flux [12,27,28]. Each of these mixtures was warmed to 1180°C, then cooled (2°C/h) followed by a decanting of the FeAs excess flux at 1090°C. Two different reaction loading ratios were used to obtain EuFe₂As₂ single crystals with different T_N . A loading ratio of Eu:FeAs= 1:5 gives an onset transition temperature of T_N = 195 K (we call 'crystal **a**'), while Eu:FeAs= 1:4

gives crystals with $T_{\rm N}=175~{\rm K}$ ('crystal **b**'). The chemical composition of these crystals was measured with a Hitachi S3400 scanning electron microscope operating at 20 kV. Three spots (each ~80 µm area) were checked and averaged on each crystal; energy-dispersive x-ray spectroscopy (EDS) and site-refinement of single-crystal X-ray diffraction analyses indicate that both crystals are stoichiometric and are EuFe₂As₂. The phase purity of the crystals was checked by collecting data on an X'Pert PRO MPD X-ray powder diffractometer; structures were solely identified as tetragonal ThCr₂Si₂ structure type (I4/mmm, Z=2).

Specific heat data were collected on EuFe₂As₂ single crystals, using a Quantum Design Physical Property Measurement System (PPMS); the C(T) results are shown in **Fig. 1a**. Each EuFe₂As₂ crystal exhibits two transitions: an ordering of Fe lattice at higher temperature, followed by lower temperature ordering (\approx 21 K) due to Eu moments. The EuFe₂As₂ 'crystal a' exhibits the higher onset ordering temperature of $T_N = 195$ K with a broader peak, compared to 'crystal b' giving a sharp lambda transition below $T_N = 175$ K. The specific heat result of 'crystal a' looks very similar to that reported in a pressed polycrystalline sample (with respect to peak width, height, and transition temperature) [20].

To analyze crystal structures, single crystal X-ray diffraction data were collected at room temperature on a Rigaku XtaLAB PRO diffractometer (Mo Source, K_{α} =0.71073 Å) equipped with a DECTRIS Pilatus 200K area detector. Data collection and reduction used the CrysAlisPro program [29]. Crystal structure refinements were performed using the SHELX-2014 program [30]. Fig. 1b (insets) shows the pictures of crystals for the data collection, stuck on top of needles. Crystals 'a' and 'b' visually looked the same, with sheet morphologies and dimensions of $\sim 0.15 \times 0.15 \times 0.02$ mm³ or smaller in a, b, and c crystallographic directions, respectively, [001] direction perpendicular to the plane of the plate. Fig. 1b gives the precession images of [HK0] and [H0L] reciprocal lattice planes, showing lattice strain effects associated with smeared diffraction spots in the L direction for 'crystal a'; this result may explain the broader feature of C(T) peak $(T_N = 195 \text{ K})$ for Fe ordering. A broader peak of specific heat is usually consistent with lattice strain and disorder. **Table 1** shows the lattice parameters and refinement results of the X-ray structure measured at room temperature. EuFe₂As₂ sample with higher T_N ('crystal a') gives lower overall a-lattice parameter and a shorter planar Fe-Fe distance of 2.7692(2) Å, indicating a contraction of 0.0053(4) Å for the in-plane Fe-Fe bond when compared to that of 2.7745(3) Å for the lower T_N ('crystal b').

Table 1: Single-crystal X-ray diffraction refinement on the two crystals of EuFe₂As₂: 'crystal a' ($T_N = 195 \text{ K}$), 'crystal b' ($T_N = 175 \text{ K}$).

EuFe ₂ As ₂ sample ID	'Crystal a'	'Crystal b'
a (Å)	3.9162(3)	3.9238(4)
c (Å)	12.104(3)	12.105(2)
arsenic at $(0, 0, z)$; 4e		
Z	0.36255(11)	0.36256(13)
$U_{ m iso}$	0.0109(6)	0.0104(6)
arsenic height, Å	1.3625(17)	1.3625(13)
iron at $(\frac{1}{2}, 0, \frac{1}{4})$; 4d		
$U_{ m iso}$	0.0164(10)	0.0137(8)
Fe-Fe distance, Å	2.7692(2)	2.7745(3)

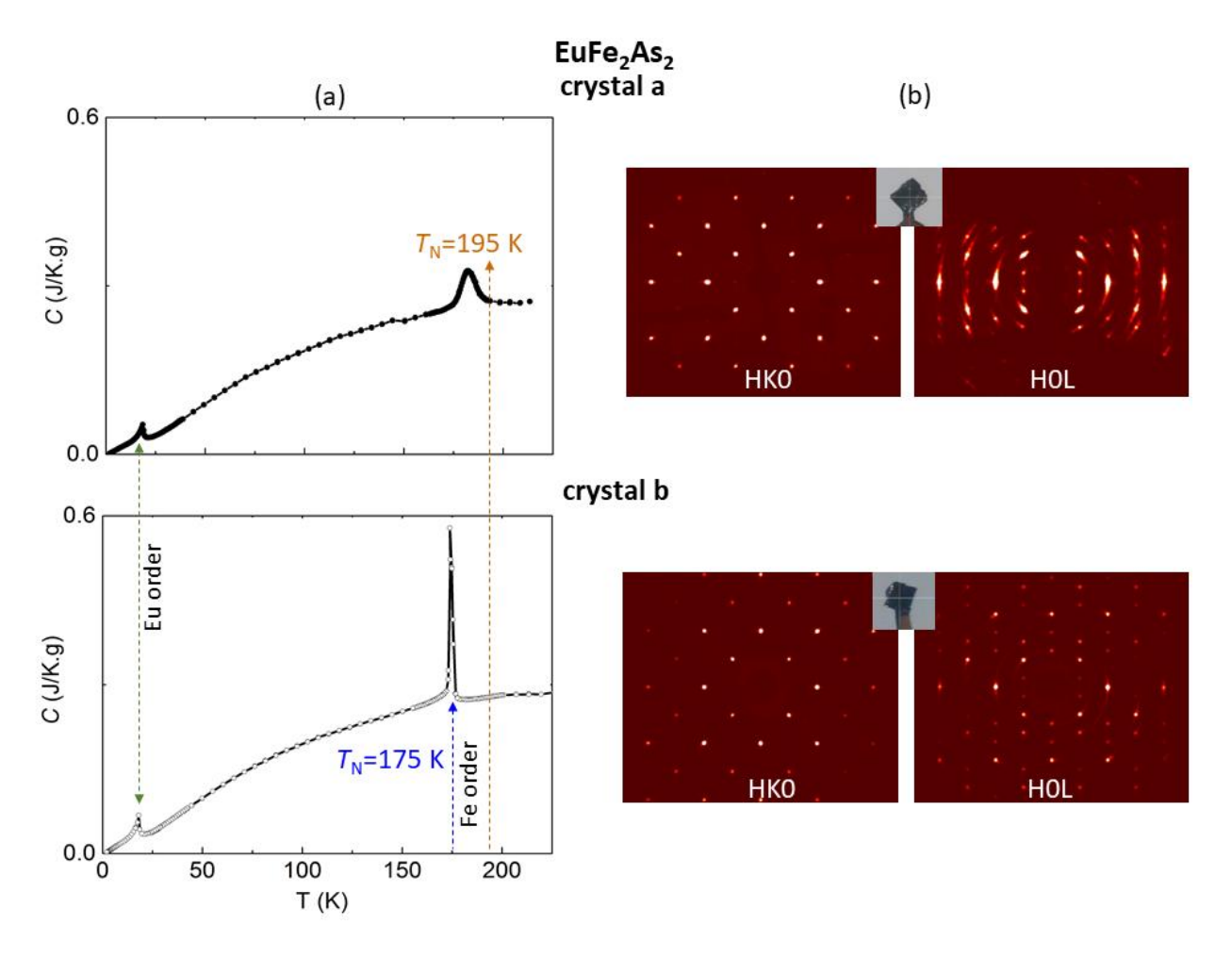


Fig. 1: Results of EuFe₂As₂ 'crystal a' and 'crystal b'. (a) Specific heat measurements with transitions associated with Eu ($T_N \approx 21$ K) and Fe ordering ($T_N = 195$ K or 175 K), C(T). (b) Precession images showing the [HK0] and [H0L] reciprocal lattice planes reconstructed from single crystal X-ray diffraction patterns measured at room temperature. Smearing in diffraction spots are more prevalent and are noted for image [H0L] in 'crystal a'.

Neutron diffraction measurements were carried out using the TOPAZ single crystal diffractometer at the ORNL Spallation Neutron Source (SNS), which uses the wavelength-resolved Laue technique with an extensive array of neutron time-of-flight area detectors for efficient 3-dimentional Q space mapping of Bragg and diffuse scattering patterns originating from magnetic and nuclear phase transitions [31]. EuFe₂As₂ 'crystal a' and 'crystal b' had dimensions of $3.25\times2.50\times0.20~\text{mm}^3$ and $2.75\times2.63\times0.30~\text{mm}^3$, respectively, and were attached on a MiTegen loop using super glue for data collection at room temperature and 95 K. Each of the samples was oriented with high precision for volumetric sampling of Bragg peaks in specific directions with the CrystalPlan program [32]. At room temperature, the $(0~2~0)_{\text{Tetragonal}}$ peak profiles for the two EuFe₂As₂ crystals are shown in **Fig. 2**, demonstrating the peak false-color maps and their corresponding peak intensity profiles along the crystallographic c-direction. The peak from 'crystal a' is broad and shows extensive diffuse lines along the L direction, which is consistent from that observed in X-ray diffraction, and gives broader and higher T_N in C(T).

As shown in **Fig. 1b** and **Fig. 2**, the streaks for the $(2\ 0\ 0)$ peak along L direction for 'crystal a' is much more pronounced than that of 'crystal b', which could be induced by strain, stacking fault or formation of antiphase boundaries in the bulk single crystal sample. Since the refined average c lattice parameter remains unchanged for both crystals (**Table 1**), the much more pronounced streaks for 'crystal a' are likely from microstrain caused by randomly distributed defects in the sample, which is evident from scanning tunneling microscopy/spectroscopy (STM/S) measurement (see below). The split of peak along c also indicates twinning and multidomain structures of 'crystal a'. The difference in terms of full-width at half maximum (FWHM) for the $(2\ 0\ 0)$ peak along L direction is about 0.13-0.27 reciprocal lattice units from that of 'crystal b', corresponding to $\sim 2\%-5\%$ variation in lattice constant c.

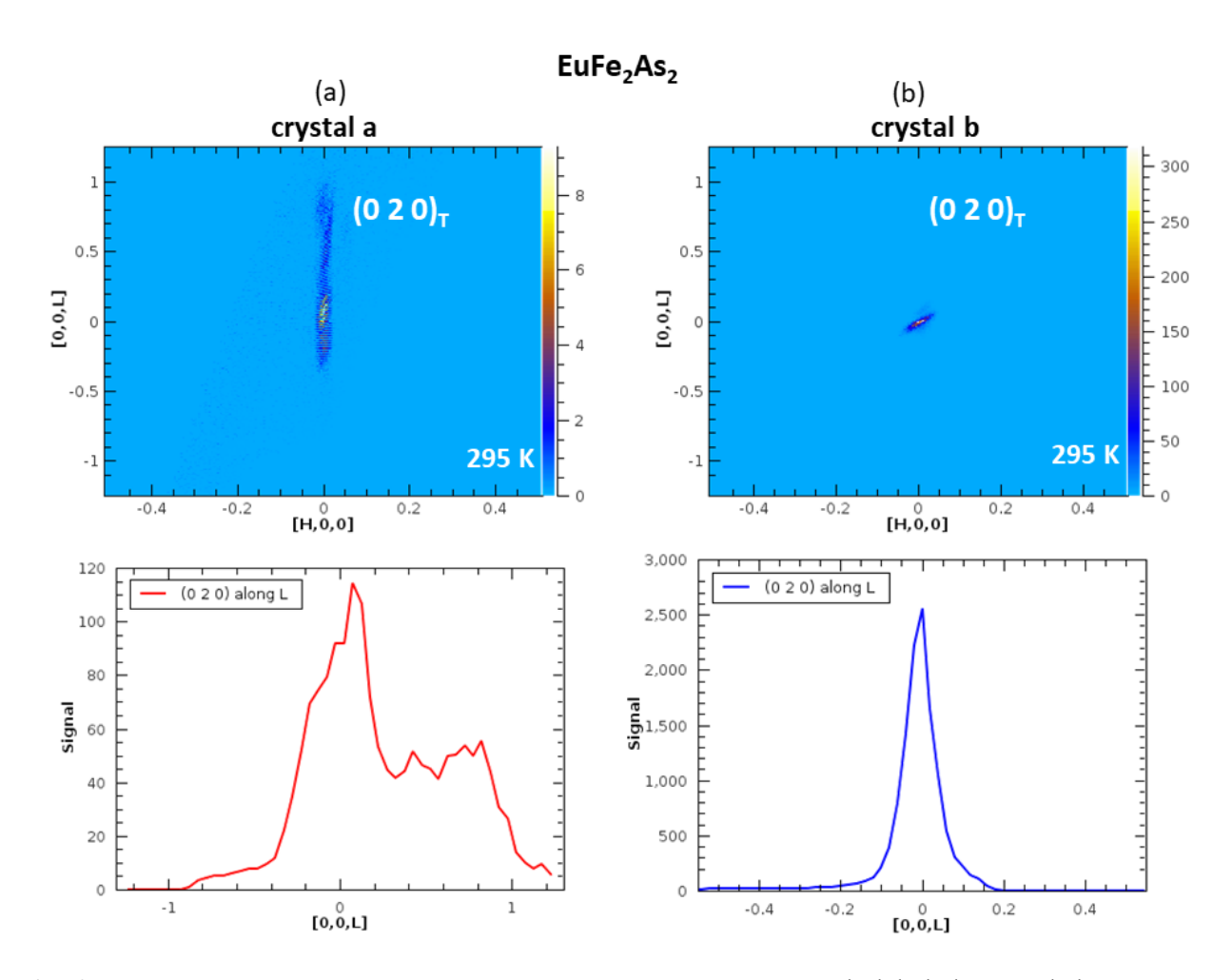


Fig. 2: Tetragonal (0 2 0) peak profiles for the two EuFe₂As₂ crystals labeled 'a' and 'b' at room temperature, showing the peak false color maps, and their corresponding peak intensity profiles along the crystallographic c direction. The peak from 'crystal a' is broadened showing extended diffuse lines.

For these crystals, neutron diffraction results were additionally carried out at 95 K, to confirm the Fe magnetic peak below T_N in accordance with the propagation vector $\mathbf{q} = (1\ 0\ 1)_{\text{Orthorhombic}} = (\frac{1}{2})_{\text{Orthorhombic}}$

 $\frac{1}{2}$ 1)_{Tetragonal} and the 'stripe' arrangement of Fe spin lattice [5-8]. (see Figure **S1a** in Supplementary). Additionally, variable temperature scans of the Eu magnetic peak at (0 3 0) for both crystals were performed below 30 K using the elastic diffuse scattering spectrometer CORELLI at SNS [33] and showed the same temperature dependence of Eu magnetic peak as (0 3 0) with $T_N \approx 21$ K (see Figure **S2**). In contrast, the Néel transition temperature for Fe is clearly lattice sensitive. The high-temperature phase transition is related to the transition metal Fe moments, whereas the low-temperature phase transition is due to magnetic ordering of localized Eu moments [23].

To find more clues in the local origin of the global/bulk $T_{\rm N}$ differences between the two EuFe₂As₂ crystals, surface topography and electronic structures were investigated using STM/S on in-situ low-temperature cleaved surfaces. The two sets of EuFe₂As₂ 'crystal a' and 'crystal b' were cleaved in an ultra-high vacuum (UHV) at ~ 78 K and then immediately transferred to the STM/S head precooled to 4.2 K without breaking vacuum. The STM/S experiments were carried out using scanning tunneling microscope with base pressure better than 2×10⁻¹⁰ Torr, with mechanically cut Pt-Ir tip. All Pt-Ir tips were conditioned on clean Au (1 1 1) and checked using the topography, surface state and work function of Au (1 1 1) before each measurement. The STM/S were controlled by the SPECS Nanonis control system. Topographic images were acquired in constant current mode with bias voltage applied to samples, and tip grounded. All the spectroscopies were obtained using the lock-in technique with a modulation of 1 mV at 973 Hz on bias voltage, dI/dV. Current-imaging-tunneling-spectroscopy were collected over a grid of pixels at bias ranges around Fermi level using the same lock-in amplifier parameters. The survey on multiple large areas of both samples shows the coexistence surface reconstructions on 'crystal a' and 'crystal b', as shown in Fig. 3. Using a similar method as STM report on Co-doped BaFe₂As₂ [34], the 2 \times 1 and $\sqrt{2}$ \times $\sqrt{2}$ reconstructed surfaces can be assigned to arsenic termination and europium termination, respectively, as shown in Fig. 3a. While the 2×1 surfaces (As termination) of both crystals (**Fig. 3b, c**) are very similar, the $\sqrt{2} \times \sqrt{2}$ surfaces (Eu termination) of the two crystals (Fig. 3d, e) are starkly different. The atomic resolved images in the insets of **Fig. 3d** and **e** from the well-ordered $\sqrt{2} \times \sqrt{2}$ reconstructed areas of the two crystals are similar, but the arrangement of the defects on surfaces is different. In 'crystal a', surface defects (one of the defects is marked with a black arrow in Fig. 3d) are basically randomly distributed on the surface, but in 'crystal b', large amount of defects prefer to form into chains (one of the chains is marked with a white arrow in Fig. 3e). By analyzing atomically resolved images around these areas, we found the chains are aligned on the antiphase boundaries. Because the surface is 2×1 or $\sqrt{2} \times \sqrt{2}$, those domains can shift by 1 to form antiphase boundaries. Although antiphase boundaries also exist on the 'crystal a' surface (one of the antiphase boundaries is marked with a green arrow in Fig. 3d), defects in 'crystal a' do not segregate along the boundaries. The electronic properties revealed by the STS from the surfaces are consistent with the morphological observation. In Fig. 3f, the average electronic local density of states (LDOS) of 2×1 surfaces (As termination) over large areas are almost identical for both crystals, but the LDOS from the two $\sqrt{2} \times \sqrt{2}$ surfaces (Eu termination) in Fig. 3g have significant differences. This reveals that the different arrangement of the surface defects in the two crystals changes the electronic structure dramatically, which can be reflective of the defects in the bulk crystals. As it is further demonstrated by the local structure analyses on both crystals (Fig. S2), and although the two crystals have a similar number of defects, their segregation around the antiphase boundaries in 'crystal b' largely decreases the amount of randomized defects on the surface that potentially lowers the LDOS.

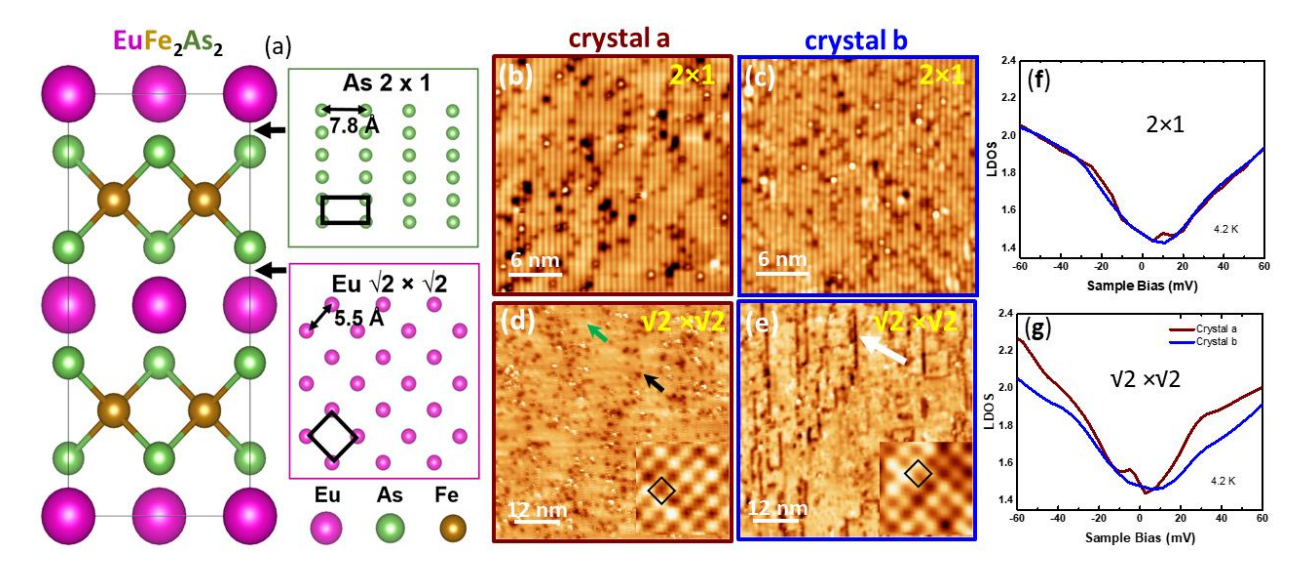


Fig. 3: (a) The structure model of EuFe₂As₂ and the surface reconstruction models of As 2×1 and Eu $\sqrt{2} \times \sqrt{2}$ termination. The black boxes outline the unit cells. (b, c) Topographic images of 2×1 surface reconstruction from 'crystals a' (-500 mV, 100 pA) and 'crystal b' (-1 V, 100 pA), respectively. (d, e) Topographic images of $\sqrt{2} \times \sqrt{2}$ surface reconstruction from 'crystals a' (-60 mV, 400 pA) and 'crystal b' (-20 mV, 800 pA), respectively. Insets show the atomic resolved images in 3×3 nm² size and black boxes are the unit cells of $\sqrt{2} \times \sqrt{2}$ surface reconstruction. (f, g) Comparison of average LDOS from 'crystals a' (red) and 'crystal b' (blue), for 2×1 and $\sqrt{2} \times \sqrt{2}$ surface reconstruction at 4.2 K.

To understand the sample-to-sample variation in Néel temperatures, we have conducted first principles theory calculations of the effect of nano-scale strain on the magnetic order, specifically on the strength of interlayer coupling. First principles calculations were performed using the linearized augmented plane wave (LAPW) density functional theory code WIEN2K [35]. As in our previous work [14] we have used the local density approximation (LDA), with arsenic height and lattice parameters taken directly from our experimental XRD refinements (**Table 1**), except as stated below. An RK_{max} value of 8.0 – the product of the smallest sphere radius and largest planewave expansion wavevector – was used. To avoid the generally unnecessary complexities of 4*f* physics we have followed our previous theoretical work [36] and performed the all-electron calculations with the substitution of Sr for the divalent Eu. Sphere radii of 2.5 Bohr were used for Sr, and between 2.26 and 2.3 for Fe (depending on volume), and between 2.15 and 2.22 for As. Identical sphere radii were used for the calculations at given volume, relevant for assessing the interlayer coupling.

Fig. 2a, showing a neutron scan of crystal 'a' along the [00L] direction, shows clear evidence of disorder, with a rather broadened peak around the (0 0 0) point and a substantial shoulder

extending most of the distance along the [001]. While there are many possible sources of such disorder, ranging from vacancies and anti-site defects (both unlikely here) to small grain sizes (unlikely given the asymmetry in **Fig. 2a**), here we explore the idea that c-axis strain in 'crystal a' is ultimately responsible for the rather broad neutron diffraction peaks. We have therefore conducted calculations of the interlayer magnetic coupling. Here we report the energy difference, per unit cell, between the ground-state 'stripe' magnetic order (which is antiferromagnetically coupled along the c-axis) and a state with ferromagnetic c-axis coupling. We have done this at the experimental lattice parameter of 12.104 Å, and in addition for c values 5% larger and smaller than this value. For the experimental c-lattice parameter, we find an interlayer coupling energy difference of 7.1 mRyd/u.c., which increases slightly to 7.7 mRyd for the +5% c value, but decreases sharply to some 4.5 mRyd for the -5% c value. These values are in qualitative agreement with the previous work on BaFe₂As₂ [37], where it was found that the application of pressure decreases the interlayer coupling. We mention also that the calculated magnetic moments decrease substantially for the smaller cell, and correspondingly increase for the larger cell. In the antiferromagnetically coupled layer state, for the smallest cell these moments are 1.25 μ_B per Fe, for the experimental cell the value is 1.63 μ_B , and for the largest cell is 1.92 μ_B .

The point of these results is that interlayer strain can plausibly affect the magnetism in a substantial manner, consistent with the disordered lattice evident in **Fig. 2a** and the observed onset temperature. What is more difficult to understand is the apparent onset increase in T_N with disorder – i.e., 'crystal a' compared with 'b'. This is particularly true given that the strained calculations show larger *decreases* in magnetic order (measured as the interlayer coupling) with *compressive* strain than increases with tensile strain. Note also that our calculations of the magnetic ordering energy, defined as the difference in energy between the stripe ground state and 'checkerboard' excited state, find no significant difference (< 1 %) resulting from the small *planar* lattice parameter change from 'crystal a' to 'b' (the experimental structures were used here), so that this planar lattice change does not appear to be the source of the Néel temperature variation. We speculate that there may be other, unascertained, forms of disorder that are active and ultimately driving this anomalous behavior.

For both EuFe₂As₂ single crystals, high-pressure electrical-resistance measurements were performed using a diamond anvil cell (see **Fig. S3a-d**), similar to our earlier reports [38-40]. Although there are reports of the application of pressure on EuFe₂As₂ causing suppression of T_N and superconductivity onset at pressure values of ~ 2 to 3 GPa [41,42], here we want to explore the differences of pressure effects on the two crystals with different T_N . A steatite pressure medium was employed in the electrical resistance measurements to assure some pressure uniformity. The temperature dependence of resistivity results is shown in **Fig. S3e**, up to ~ 20 GPa. For these crystals, clear anomalies due to Fe and Eu ordering are seen in the data. Although the feature due to Eu ordering is not changed for either crystals up to ~ 4 GPa, Fe ordering is greatly sensitive to pressure and the rate of T_N suppression for both crystals is similar. For 'crystal b' with smaller T_N = 175 K, the drop is resistivity is noticed at lower pressure of 2.5 GPa, compared to 'crystal a,' with T_c setting in at 3.2 GPa. EuFe₂As₂ with sharper, but lower T_N , gives a slightly higher superconducting dome, summarized in T-P phase diagram for both crystals in **Fig. 4**.

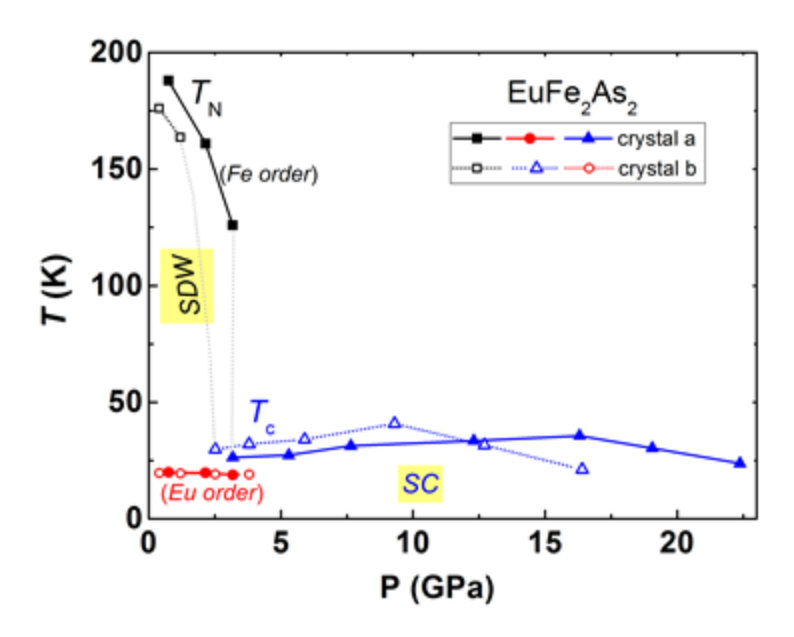


Fig. 4: Temperature-pressure phase diagram for the two EuFe₂As₂ crystals with different T_N at ambient pressure.

We find that, depending on disorder-related lattice variability, significantly different Fe Néel ordering temperatures exist in the stoichiometric EuFe₂As₂ crystal. We additionally find that while the a-crystallographic lattice value affects the strength of spin interactions, the c-lattice parameter is most crucial in determining the value of the overall $T_{\rm N}$. The diffuse scattering that is seen along the [00L] direction in X-ray and neutron diffraction measurements for the higher ordering temperature crystal may well be the origin of the broadened specific heat peak and probably a cause for the suppressed superconducting dome. The surface topography and electronic structure studies show that there is a clear difference in electronic and defect structures between the two $T_{\rm N}$ crystals, with defect states dominating and elevating the LDOS for higher $T_{\rm N}$ 'crystal a'. Although the two crystals have a similar number of defects, their segregation around the antiphase boundaries in 'crystal b' largely decreases the amount of individual defects on the surface, which may potentially produce a better superconductor. This study thereby demonstrates the tuning of $T_{\rm N}$ in an iron arsenide by controlled disorder, and can explain ordering temperature variations for such stoichiometric quantum materials in literature.

This manuscript has been authored by UT-Battelle, LLC under Contract No. DE-AC05-00OR22725 with the U.S. Department of Energy. The United States Government retains and the publisher, by accepting the article for publication, acknowledges that the United States Government retains a non-exclusive, paid-up, irrevocable, world-wide license to publish or reproduce the published form of this manuscript, or allow others to do so, for United States Government purposes. The Department of Energy will provide public access to these results of federally sponsored research in accordance with the DOE Public Access Plan.

The research is primarily supported by the U.S. Department of Energy (DOE), Office of Science, Basic Energy Sciences (BES), Materials Science and Engineering Division. Neutron scattering experiments at Oak Ridge National Laboratory (ORNL) were supported by the Scientific User Facilities Division, Office of BES, DOE. Also, Y. V. and G. K. acknowledge support from the U.S. National Science Foundation (NSF) under Grant No. DMR-1608682.

- [1] A. S. Sefat, and D. J. Singh, MRS Bull. **36**, 614 (2011).
- [2] I. R. Fisher, L. Degiorgi, and Z. X. Shen, Rep. Prog. Phys. 74, 124506 (2011).
- [3] J. L. Niedziela, M. A. McGuire, and T. Egami, Phys. Rev. B 86, 174113 (2012).
- [4] H. Ding, P. Richard, K. Nakayama, K. Sugawara, T. Arakane, Y. Sekiba, A. Takayama, S. Souma, T. Sato, T. Takahashi, Z. Wang, X. Dai, Z. Fang, G. F. Chen, J. L. Luo, and N. L. Wang, Europhys. Lett. **83**, 47001 (2008).
- [5] Q. Huang, Y. Qiu, W. Bao, M. A. Green, J. W. Lynn, Y. C. Gasparovic, T. Wu, G. Wu, and X. H. Chen, Phys. Rev. Lett. **101**, 257003 (2008).
- [6] J. Zhao, W. Ratcliff, J. W. Lynn, G. F. Chen, J. L. Luo, N. L. Wang, J. P. Hu, and P. C. Dai, Phys. Rev. B 78, 140504 (2008).
- [7] A. I. Goldman, D. N. Argyriou, B. Ouladdiaf, T. Chatterji, A. Kreyssig, S. Nandi, N. Ni, S. L. Bud'ko, P. C. Canfield, and R. J. McQueeney, Phys. Rev. B **78** 100506 (2008).
- [8] Y. Xiao, Y. Su, M. Meven, R. Mittal, C. M. N. Kumar, T. Chatterji, S. Price, J. Persson, N. Kumar, S. K. Dhar, A. Thamizhavel, and Th. Brueckel, Phys. Rev. B **80**, 174424 (2009).
- [9] W.-L. Zhang, A. S. Sefat, H. Ding, P. Richard, and G. Blumberg, Phys. Rev. B **94**, 014513 (2016).
- [10] J.-H. Chu, H.-H. Kuo, J. G. Analytis, and I. R. Fisher, Science 337, 710 (2012).
- [11] M. Rotter, M. Tegel, D. Johrendt, I. Schellenberg, W. Hermes, and R. Pöttgen, Phys. Rev. B **78**, 020503 (2008).
- [12] A. S. Sefat, R. Jin, M. A. McGuire, B. C. Sales, D. J. Singh, and D. Mandrus, Phys. Rev. Lett. **101**, 117004 (2008).
- [13] B. Saparov, and A. S. Sefat, Dalton Trans. **43**, 14971 (2014).
- [14] L. Li, Q. Zheng, Q. Zou, S. Rajput, A. O. Ijaduola, Z. Wu, X. P. Wang, H. B. Cao, S. Somnath, S. Jesse, M. Chi, Z. Gai, D. Parker, and A. S. Sefat, Sci. Rep. 7, 949 (2017).
- [15] G.-F. Chen, Z. Li, G. Li, W.-Z. Hu, J. Dong, J. Zhou, X.-D. Zhang, P. Zheng, N. -L. Wang, and J.-L. Luo, Chin. Phys. Lett. **25**, 3403 (2008).
- [16] J. Zhao, W. Ratcliff II, J. W. Lynn, G. F. Chen, J. L. Luo, N. L. Wang, J. Hu, and P. Dai, Rev. B **78**, 140504 (2008).
- [17] S. R. Saha, N. P. Butch, K. Kirshenbaum, J. Paglione, and P. Y. Zavalij, Phys. Rev. Lett. **103**, 037005 (2009).
- [18] B. Saparov, C. Cantoni, M. Pan, T. C. Hogan, W. Ratcliff II, S. D. Wilson, K. Fritsch, M. Tachibana, B. D. Gaulin, and A. S. Sefat, Sci. Rep. 4, 4120 (2014).

- [19] K. Gofryk, B. Saparov, T. Durakiewicz, A. Chikina, S. Danzenbächer, D. V. Vyalikh, M. J. Graf, and A. S. Sefat, Phys. Rev. Lett. **112**, 186401 (2014).
- [20] Z. Ren, Z. Zhu, S. Jiang, X. Xu, Q. Tao, C. Wang, C. Feng, G. Cao, and Z. Xu, Phys. Rev. B **78**, 052501 (2008).
- [21] Y. Xiao, Y. Su, M. Meven, R. Mittal, C. M. N. Kumar, T. Chatterji, S. Price, J. Persson, N. Kumar, S. K. Dhar, A. Thamizhavel, and Th. Brueckel, Phys. Rev. B **80**, 174424 (2009).
- [22] J. Herrero-Martín, V. Scagnoli, C. Mazzoli, Y. Su, R. Mittal, Y. Xiao, T. Brueckel, N. Kumar, S. K. Dhar, A. Thamizhavel, and L. Paolasini, Phys. Rev. B **80**, 134411 (2009).
- [23] H. S. Jeevan, Z. Hossain, D. Kashinathan, H. Rosner, C. Geibel and P. Gegenwart, Phys. Rev. B 78, 5 (2008).
- [24] S. Zapf, C. Stingl, K.W. Post, J. Maiwald, N. Bach, I. Pietsch, D. Neubauer, A. Löhle, C. Clauss, S. Jiang, H. S. Jeevan, D. N. Basov P. Gegenwart, and M. Dressel, Phys. Rev. Lett. 113, 227001 (2014).
- [25] K. Matsubayashi, K. Munakata, M. Isobe, N. Katayama, K. Ohgushi, Y. Ueda, N. Kawamura, M. Mizumaki, N. Ishimatsu, M. Hedo, I. Umehara, and Y. Uwatoko, Phys. Rev. B. **84**, 024502 (2011).
- [26] U. B. Paramanik, Debarchan Das, R. Prasad, and Z. Hossain, J. Phys.: Condes. Matter 25, 265701 (2013).
- [27] B. Saparov, J. E. Mitchell, and A. S. Sefat, Supercond. Sci. Technol. 25, 084016 (2012).
- [28] A. S. Sefat, Curr. Opin. Solid State & Mater. Sci. 17, 59 (2013).
- [29] CrysAlisPro 1.171.39.9g, Rigaku Oxford Diffraction (2017)
- [30] G. M. Sheldrick, Acta Cryst. C 71, 3 (2015).
- [31] A. J. Schultz, M. R. V. Jorgensen, X. Wang, R. L. Mikkelson, D. J. Mikkelson, V. E. Lynch, P. F. Peterson, M. L. Green, and C. M. Hoffmann, J. Appl. Crystallogr. **47**, 915 (2014).
- [32] T. M. Michels-Clark, A. T. Savici, V. E. Lynch, X. P. Wang, and C. M. Hoffmann, J. Appl. Crystallogr. 49, 497 (2016).
- [33] F. Ye, Y. Liu, R. Whitfield, R. Osborn, and S. Rosenkranz, J. Appl. Crystallogr. 51, 315 (2018).
- [34] Q. Zou, Z. M. Wu, M. M. Fu, C. M. Zhang, S. Rajput, Y. P. Wu, L. Li, D. S. Parker, J. Kang, A. S. Sefat, and Z. Gai, Nano Letters 17, 1642 (2017).
- [35] P. Blaha, K. Schwarz, G. K. H. Madsen, D. Kvasnicka, J. Luitz, R. Laskowski, F. Tran and L. D. Marks, WIEN2k, An Augmented Plane Wave + Local Orbitals Program for Calculating Crystal Properties (Karlheinz Schwarz, Techn. Universität Wien, Austria), 2018. ISBN 3-9501031-1-2
- [36] S. J. Moon, J. H. Shin, D. Parker, W. S. Choi, I. I. Mazin, Y. S. Lee, J. Y. Kim, N. H. Sung, B. K. Cho, S. H. Khim, J. S. Kim, K. H. Kim, and T. W. Noh, Phys. Rev. B **81**, 205114 (2010).
- [37] M. D. Johannes, I. I. Mazin, and D. S. Parker, Phys. Rev. B 82, 024527 (2010).
- [38] S. T. Weir, J. Akella C. A. Ruddle, Y. K. Vohra and S. A. Catledge, Appl. Phys. Lett. **77**l, 3400 (2000).
- [39] Y. K. Vohra and S. T. Weir, High pressure phenomenon Proc. Int. School of Physics—Enrico Fermi, Course XXLVII, Ed. R. J. Hemley, G. L. Chiarotti, M. Bernasconi, L. Ulivi (Bologna: IOS Press), p 87 (2002).
- [40] G. Tsoi, A. Stemshorn, Y. K. Vohra, P. M. Wu, F. C. Hsu, Y. L. Huang, M. K. Wu, K. W. Yeh, and S. T. Weir, J. Phys: Condens Matter. **21**, 232201(2009).
- [41] C. F. Miclea, M. Nicklas, H. S. Jeevan, D. Kasinathan, Z. Hossain, H. Rosner, P. Gegenwart, C. Geibel, and F. Steglich, Phys. Rev. B **79**, 212509 (2009).
- [42] T. Terashima, M. Kimata, H. Satsukawa, A. Harada, K. Hazama, S. Uji, H. S. Suzuki, T. Matsumoto, and K. Murata, J. Phys. Soc. Jpn. **78**, 083701 (2009).

Supplementary Material

for

Lattice Disorder Effect on Magnetic Ordering of Iron Arsenides

A. S. Sefat, X. P. Wang, Y. Liu, D.S. Parker, Q. Zou, M. M. Fu, Z. Gai, G. Kalaiselvan, Y. Vohra, L. Li

¹ Materials Science & Technology Division, Oak Ridge National Laboratory, Oak Ridge, TN 37831
 ² Neutron Scattering Division, Oak Ridge National Laboratory, Oak Ridge, TN 37831
 ³ Center for Nanophase Materials Sciences, Oak Ridge National Laboratory, Oak Ridge, TN 37831, USA
 ⁴ Department of Physics, University of Alabama at Birmingham, Birmingham, AL 35294

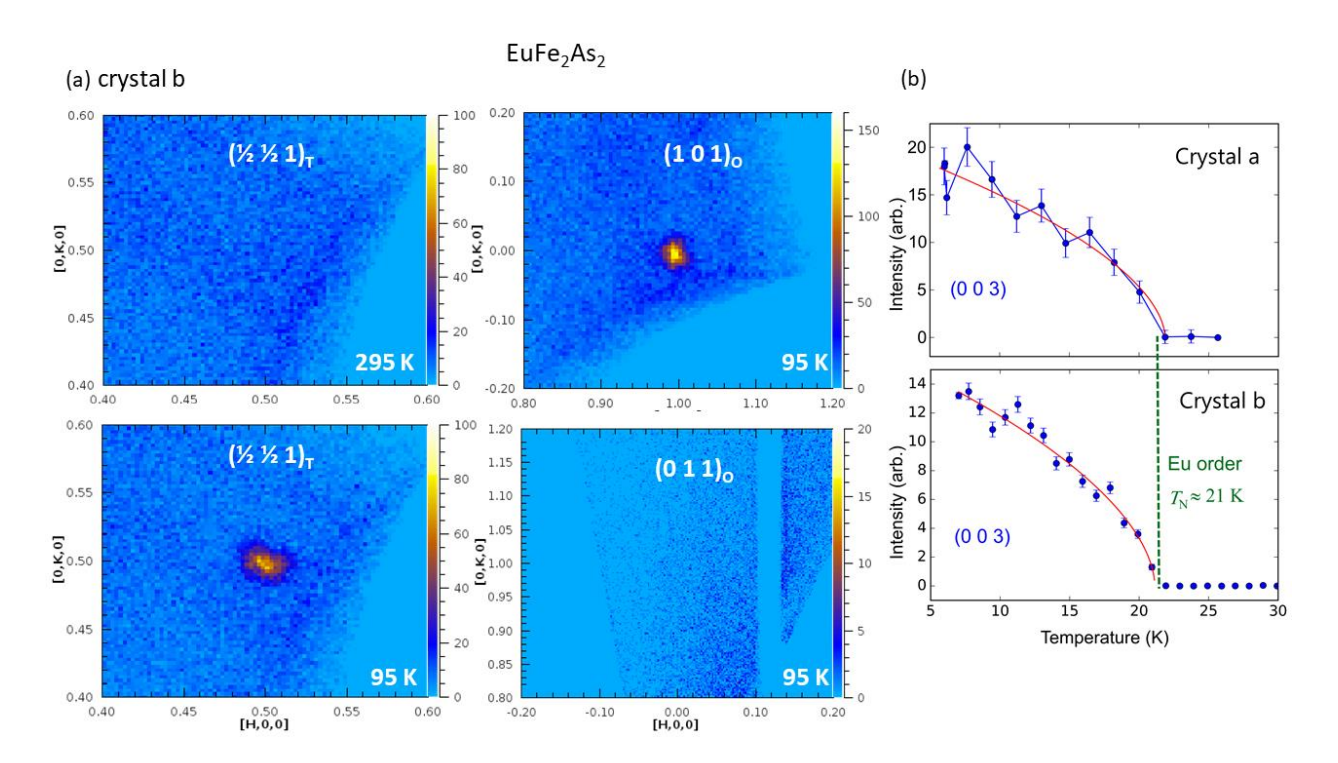


Fig. S1: (a) For EuFe₂As₂ and neutron single crystal diffraction showing the appearance of Fe magnetic peak for 'crystal b' below $T_{\rm N}$ in accordance with the propagation vector $(1\ 0\ 1)_{\rm O}=(\frac{1}{2}\ \frac{1}{2}\ 1)_{\rm T}$. Left: There is no Fe magnetic peak in the tetragonal phase at room temperature, while Fe magnetic superlattice peak is seen at 95 K indexed in $(\frac{1}{2}, \frac{1}{2}, 1)_{\rm T}$. Right: The same Fe magnetic peak indexed as $(1\ 0\ 1)_{\rm O}$ in the low temperature orthorhombic phase after basis transformation (a+b, -b+a, c), while absence of $(0\ 1\ 1)_{\rm O}$ is consistent with 'stripe' arrangement of Fe spin lattice reported for EuFe₂As₂ [8] The Fe spins are antiparallel along a- and c-axes, and parallel along b-axis. No twinned domains are observed for crystal b. (b) Temperature dependence of the Eu $(0\ 0\ 3)$ magnetic reflection for crystals 'a' and 'b'. Both samples exhibit approximately the same ordering behavior in terms of ordering temperature $(21-22\ \text{K})$ and critical exponents (0.28).

For EuFe₂As₂ crystals, neutron diffraction results were additionally carried out at 95 K using TOPAZ single-crystal diffractometer, with the temperature controlled by an Oxford CryoStream with l-N₂ flow. The appearance of an Fe magnetic peak below T_N is confirmed in accordance with the propagation vector \mathbf{q} =(1 0 1)₀=(½ ½ 1)_T. Additionally, the absence of (0 1 1)₀ reflection at temperatures below T_N are consistent with the assignment of Fe spins are antiparallel along a-and c-axes, and parallel along b-axis of the orthorhombic cell; these results are shown for 'crystal b' in **Fig. S1a**. The same EuFe₂As₂ single crystal samples 'a' and 'b' used for the TOPAZ experiments were remounted using an aluminum pin on the CORELLI cryostat for data collection below 30 K. Peak intensities for individual temperature scans used ~ 7 minutes of neutron beam time, with 0.5 Columbus of proton-charge on target as the stopping criteria for data collection at each temperature. The temperature dependent Eu magnetic peak of (0 3 0) shows approximately the same ordering for both crystals, with critical exponents 0.28(5) for 'crystal a' and 0.28(3) for 'crystal b.' These results are shown in **Fig. S1b**.

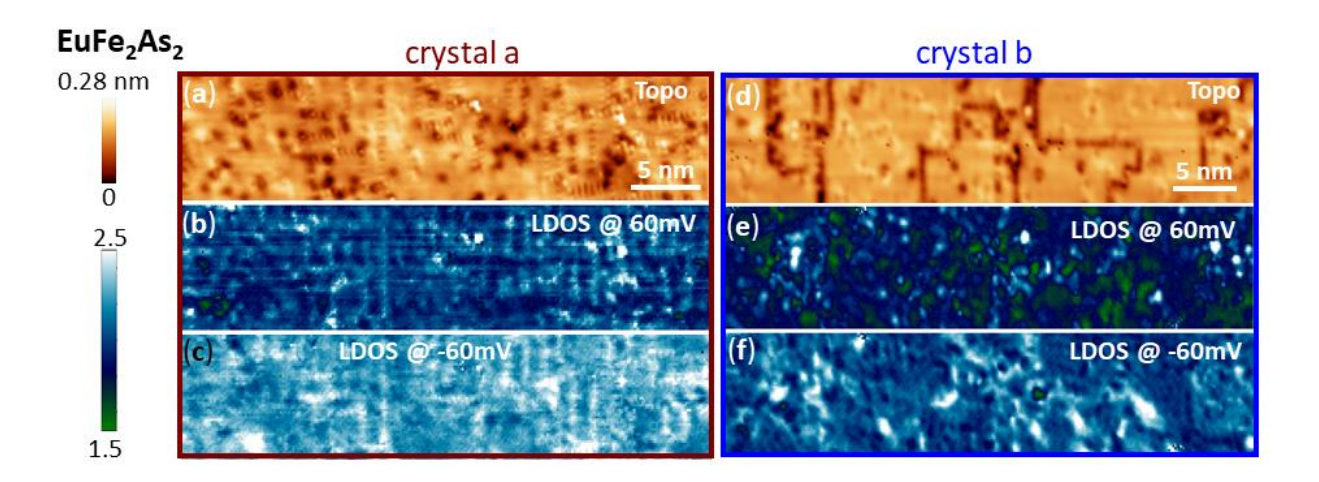


Fig. S2: EuFe₂As₂ local structures. (a, b, c) Topographic image, LDOS at 60 mV and -60 mV of $\sqrt{2} \times \sqrt{2}$ reconstructed surface on 'crystals a' (-60 mV, 800 pA). (d, e, f) Topographic image, LDOS at 60 mV and -60 mV of $\sqrt{2} \times \sqrt{2}$ reconstructed surface on 'crystal b' (-60 mV, 800 pA).

To better understand how the local chemical structure changes the electronic structure on $\sqrt{2} \times \sqrt{2}$ surfaces, the spatial distributions of LDOS at \pm 60 mV from the two crystals are plotted in **Fig. S2** along with the simultaneously acquired topographic images. For 'crystal a', the intensities of the LDOS maps (**Fig. S2b, c**) are relatively higher and more uniform compared to 'crystal b' (**Fig. S2e, f**). What marks the difference between the two crystals are the large quantities of low density-of-state areas in 'crystal b' (green areas in **Fig. S2e** and dark blue areas in **Fig. S2f**), those are areas with fewer vacancy defects in the topographic images. It is interesting to note that the LDOS intensity and influential territory around individual vacancy-defects are much higher than that of vacancy chains. This observation explains the different average LDOS in these crystals. Although the two surfaces of the crystals have a similar number of Eu vacancies, their segregation around the antiphase boundaries in 'crystal b' largely decreases the amount of individual vacancies on the surface. The relatively large amount of random individual vacancies in 'crystal a' largely elevates the density of states.

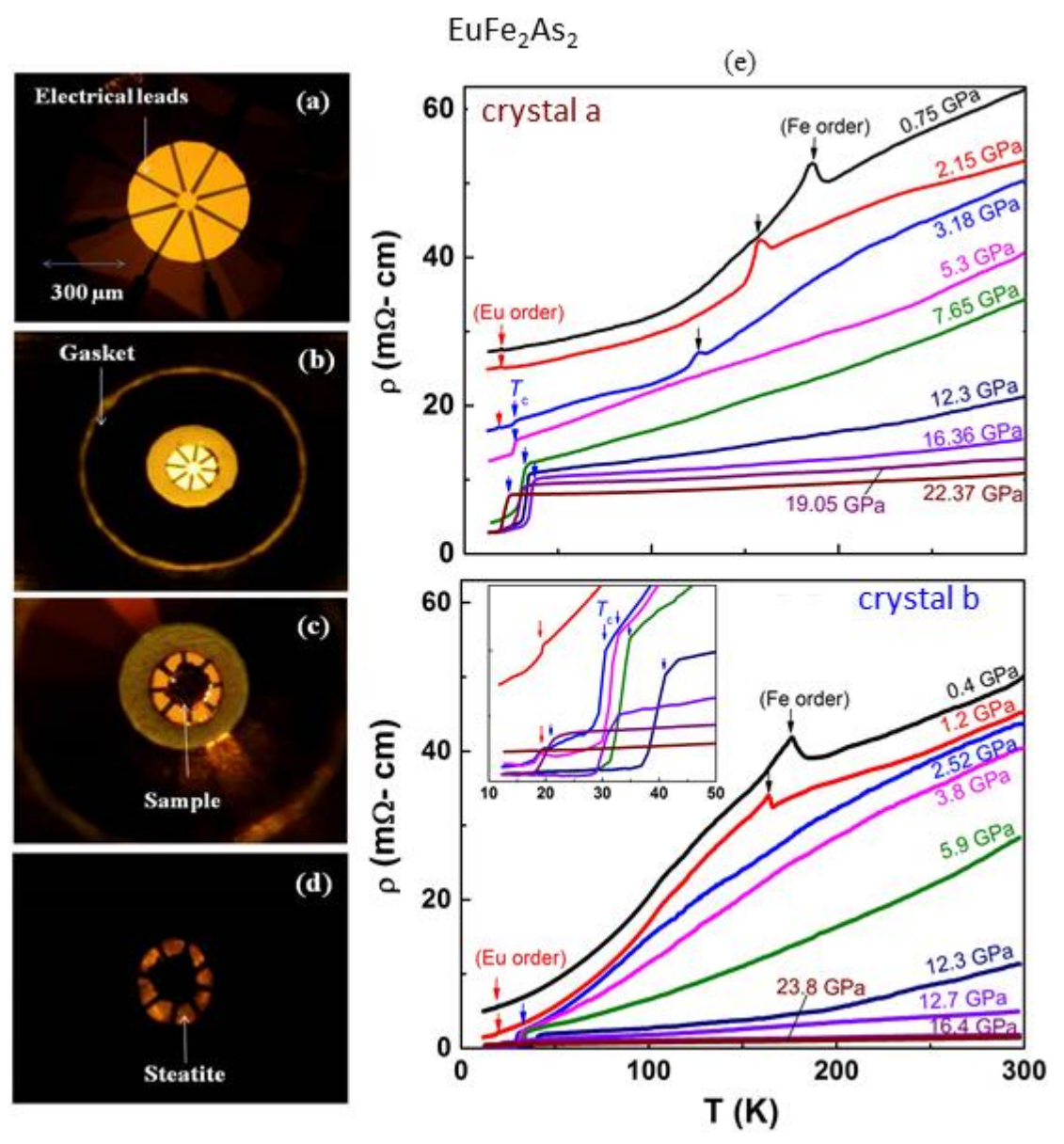


Fig. S3. (a) Eight probe designer diamond anvil used in high-pressure resistivity measurements of EuFe₂As₂ single crystal. The current and voltage contacts in the four probe electrical measurements are indicated. (a) The inset is the close-up of the diamond culet showing the eight shiny tungsten metal probes emerging near the center to make contact with the sample at high pressures. The metal probes are embedded in a chemical vapor deposited diamond layer elsewhere except for the contacts indicated. (b) Metallic gasket mounting in the designer diamond, (c) and (d) EuFe₂As₂ crystal loaded with a steatite pressure medium, thereby electrically insulating the sample from the gasket. (e) Temperature and pressure dependence of the electrical resistivity of EuFe₂As₂ 'crystal a' (top) and 'crystal b' (bottom).

For both EuFe₂As₂ single crystals, high-pressure electrical-resistance measurements were performed using a diamond anvil cell; see **Fig. S3a**. In situ, one of the anvils was symmetrically arrange and deposited with eight tungsten microprobes encapsulated in a homoepitaxial diamond film and are exposed only near the tip of the diamond to make contact with the EuFe₂As sample

at high pressure. The designer diamond anvil was beveled with flat diameter of 100 μm and culet diameter of $\sim 300~\mu m$. The distance between two opposite leads was $\sim 50~\mu m$. The gasket was made from a 240 μm thick hardened spring steel foil pre-indented to 80 μm with a 120 μm diameter hole electrospark drilled through the center of the preindented region. Apart from eight electrical leads, two leads were used to set constant current through the sample and the two additional leads were used to monitor the voltage across the sample. A steatite pressure medium was employed in the electrical resistance measurements to assure electrical insulation of the sample from metallic gasket. The pressure was monitored by the ruby fluorescence technique and care was taken to carefully calibrate the ruby R_1 and R_2 emission in both samples at low temperatures.